## RESEARCH ARTICLE

Check for updates

# Imine-linked donor–acceptor metal–organic frameworks for an efficient photocatalytic oxidative coupling reaction†

Ri-Qin Xia, [ID] Tian-E. Zhang, Zhen-Na Liu, Rong-Jia Wei, [ID] * Guo-Hong Ning [ID] * and Dan Li [ID]

Donor–acceptor metal–organic frameworks (D–A MOFs) are promising platforms for photocatalytic organic transformation and energy conversion due to their controllable chemical structures and tunable energy band gaps. Herein, we report two imine-linked D–A MOFs, namely **JNM-18** and **JNM-19**, containing both Cu(ı) cyclic trinuclear units (CTUs) as an electron acceptor (A) and triphenylbenzene (TPB) or hexaphenylbenzene (HPB) as an electron donor (D) synthesized by Schiff base condensations. With precise spatial distribution of donor and acceptor moieties within the two-dimensional (2D) networks, the obtained D–A MOFs exhibited efficient photocatalytic activity for the aerobic oxidation reaction of benzylamines upon irradiation with a violet LED. Interestingly, **JNM-18** with planar TPB moieties showed better photo-electrochemical properties, and thus better photocatalytic performance than **JNM-19** containing nonplanar HPB units with propeller arrangement which was possibly due to the stronger electron-donating abilities of the associated building units. This work illustrates a convenient approach to reticularly prepare D–A MOFs as photocatalysts by linkage of dynamic covalent bonds.

## Introduction

Metal–organic frameworks (MOFs) constructed from metal ions/clusters and bridging ligands based on reticular chemistry are rapidly developing porous crystalline materials.[1–3] Due to the high surface areas and well-defined nanopores, MOFs are highly attractive and have been broadly studied in many research fields such as guest sensing, energy storage, gas separation, and heterogeneous catalysis.[4–8] In particular, donor–acceptor MOFs (D–A MOFs) with precise spatial distribution of donor and acceptor moieties are attractive platforms for photocatalyzed organic transformation and energy conversion due to their controllable chemical structures and tunable energy band gaps.[9–11] Upon photo-irradiation, D–A MOFs can generate effectively separate electron–hole pairs that turn $O_2$ into reactive oxygen species (ROS) which can be further used to initiate the photocatalyzed oxidative reaction.[12,13] Although the photocatalyzed aerobic oxidation reactions have been widely explored using homogeneous catalysts of coordination complexes with noble metal ions in the past few decades, it is desired to develop non-noble-metal D–A MOFs as heterogeneous photocatalysts with high efficiency and recyclability.[14–17]

Cyclic trinuclear units (CTUs) are a class of functional metal clusters with coordinatively unsaturated $d^{10}$ metal ions showing unique properties such as luminescence, metallophilic attraction, π-acidity/basicity and catalytic properties.[18,19] Recently, by combining the chemistry of MOFs and covalent organic frameworks (COFs),[20] we and other groups have successfully synthesized various functional CTU-based MOFs linked by dynamic covalent bonds, which allows us to bring the merits from MOFs and COFs.[21–29] Due to the built-in characteristics, CTU-based MOFs exhibit not only highly ordered structures and controllable porosities, but also unique catalytic activity for various organic transfer reactions.[26–29] It has been found that Cu(ı) CTUs exhibited an electron-deficient surface,[30] which can be used as electron acceptor building blocks to construct D–A MOFs *via* dynamic covalent chemistry. We envision that the photocatalytic performance of Cu(ı) CTU based MOFs can be boosted through fine-tuning of organic linkers with different electron-donating capacities.[31]

In this work, we report two imine-linked two-dimensional (2D) D–A MOFs, **JNM-18** and **JNM-19** (JNM = Jinan materials), which were reticularly constructed by Schiff base reactions

College of Chemistry and Materials Science, Guangdong Provincial Key Laboratory of Functional Supramolecular Coordination Materials and Applications, Jinan University, Guangzhou, Guangdong 510632, P. R. China. E-mail: rjwei@jnu.edu.cn, guohongning@jnu.edu.cn

This journal is © the Partner Organisations 2024

*Inorg. Chem. Front.*, 2024, **11**, 417–424 | **417**

between a carboxaldehyde functionalized Cu(I) CTU as an electron acceptor and triphenylbenzene (TPB)[32,33] or hexaphenylbenzene (HPB)[34,35] moieties as electron donors, respectively (Fig. 1a). The Cu(I) CTU-based MOFs showed similar imine-linked D–A pair structures yet different framework topologies due to the varied connecting number of the donor units. With the precise spatial distribution of donor and acceptor moieties in the skeleton, **JNM-18** and **JNM-19** delivered efficient photocatalytic activity for the aerobic oxidation reaction of benzylamines. Owing to the stronger electron donating ability of the planar TPB core compared to the nonplanar HPB unit with propeller arrangement, **JNM-18** showed better photo-electrochemical properties than **JNM-19**, such as superior visible-light absorption, enhanced charge separation, and higher ROS generation efficiency, resulting in higher photocatalytic activity. This research provides a convenient approach to construct reticular D–A MOF photocatalysts by linkage of dynamic covalent bonds.

## Results and discussion

### Syntheses and characterization

Two imine-linked D–A MOFs, namely **JNM-18** and **JNM-19**, were prepared under solvothermal conditions at 120 °C for 72 h by Schiff base condensation between the Cu-CTU, **Cu₃L₃** ($HL$ = pyrazole-4-carboxaldehyde), and the corresponding amino organic linkers, 5″-(4′-amino-[1,1′-biphenyl]-4-yl)-[1,1′:4′,1″:3″,1‴:4‴,1⁗-quinquephenyl]-4,4⁗-diamine (**1**) and 3″,4″,5″,6″-tetrakis(4′-amino[1,1′-biphenyl]-4-yl)-[1,1′:4′,1″:2″,1‴:4‴,1⁗-quinquephenyl]-4,4⁗-diamine (**2**), respectively (Fig. S1 and S2, see the ESI† for details). Electrostatic potential (ESP) surface maps of **JNM-18** and **JNM-19** calculated based on their optimized structures revealed the positive potential focus on the Cu ions and the negative potential centered on the TPB and HPB cores, suggesting that a donor–acceptor heterojunction can be generated when they are linked with a covalent bond (Fig. 1b and see the ESI† for details). Moreover, the TPB core is much flatter than the HPB units with propeller arrangement.[36] This superior integrity of π-conjugation is strongly related to the electron donating ability, which leads to a stronger donor–acceptor interaction in **JNM-18** than that in **JNM-19**, influencing their photo-electrochemical properties and photocatalytic activity.[37]

The formations of imine linkages of the products were confirmed using Fourier Transform Infrared (FT-IR) spectra, as evidenced by the disappearance of the N–H stretching bands[21] ranging from 3466–3203 cm⁻¹ and the appearance of the C=N stretching signals[22] located at 1621 and 1624 cm⁻¹ for **JNM-18** and **JNM-19**, respectively (Fig. S5 and S6†). The solid-state ¹³C cross-polarization/magic-angle spinning nuclear magnetic resonance (CP/MAS NMR) spectra revealed the characteristic imine carbon[16] resonance peaks at 156 and 157 ppm for **JNM-18** and **JNM-19**, respectively, demonstrating the successful formation of C=N linkages within the frameworks (Fig. S7 and S8†). Energy-dispersive X-ray spectroscopy (EDS) elemental analyses of **JNM-18** and **JNM-19** revealed a uniform distribution of Cu ions in the networks (Fig. S9 and S10†). X-ray photoelectron spectroscopy (XPS) spectra of **JNM-18** and **JNM-19** revealed symmetrical Cu(I) 2p₃/₂ peaks at 932.98 and 932.82 eV without satellite peaks,[38] suggesting the monovalent state of copper ions within the skeleton (Fig. S11 and S12†). Thermal gravimetric analyses (TGA) and various temperature PXRD experiments revealed moderate thermal stability of **JNM-18** and **JNM-19** which remained crystalline up to 200 °C (Fig. S13–16†). The materials also showed good stabilities towards water and various organic solvents (Fig. S17 and S18†).

The high crystallinities of **JNM-18** and **JNM-19** were confirmed by powder X-ray diffraction (PXRD) shown in Fig. 2a and d, respectively, of which the structures were studied by PXRD experiments combined with theoretical simulations. For example, **JNM-18** exhibited an intense peak at 3.20○ and three small peaks at 5.78○, 6.70○, and 8.78○, which could be assigned to the (1$\bar{1}$0), (1$\bar{2}$0), (2$\bar{2}$0), and (210) planes, respectively. We further calculated the eclipsed (AA) and staggered packing (AB) modes of the 2D lamellar layers of **JNM-18** with **hcb** topology using Materials Studio (Fig. 2b and S21†). The calculated PXRD patterns based on the two possible stacking models of **JNM-18** are shown in Fig. S19,† which clearly revealed the good matching of the experimental PXRD pattern with the calculated one obtained from the AB stacking structure. Pawley refinement was thus performed based on the AB packing model, which gave a trigonal space group of $P3$ with
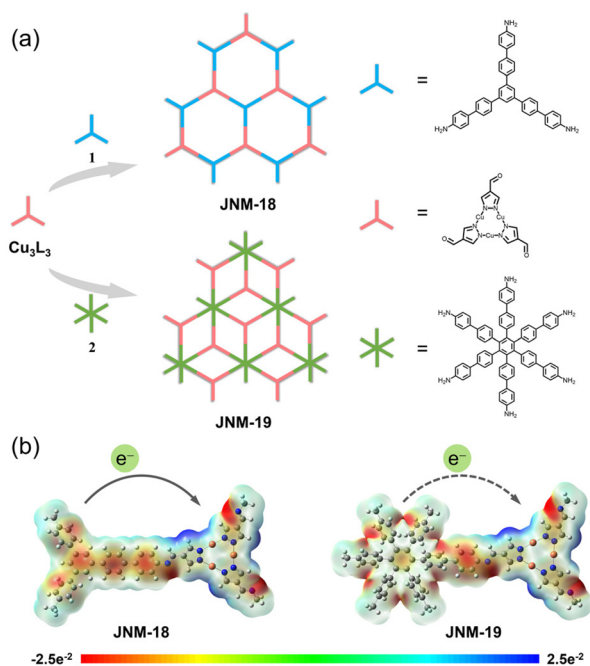


**Fig. 1** (a) Syntheses of imine-linked D–A MOFs, **JNM-18** and **JNM-19**, *via* Schiff base reactions between the Cu₃ CTU acceptor (**Cu₃L₃**) and TPB (**1**) or HPB (**2**) donors, respectively. (b) The ESP surface maps for the optimized structures of **JNM-18** (left) and **JNM-19** (right). The planar TPB moiety in **JNM-18** shows a stronger electron donating ability than the HPB unit with nonplanar propeller arrangement in **JNM-19**.
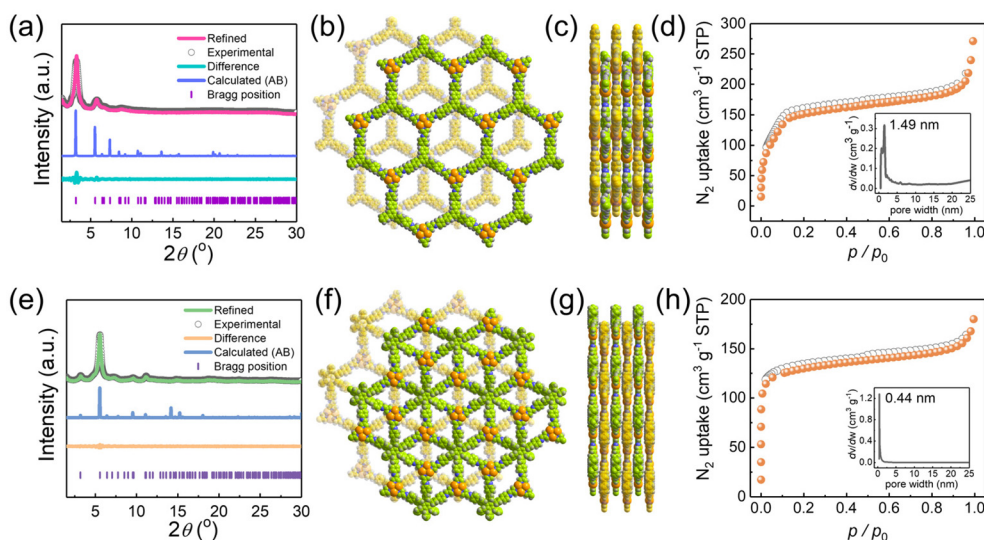
**Fig. 2** PXRD structural analyses of **JNM-18** (a) and **JNM-19** (e). Top and side views of the refined AB models of **JNM-18** (b and c) and **JNM-19** (f and g). Nitrogen adsorption (filled) and desorption (open) isotherm profiles of **JNM-18** (d) and **JNM-19** (h) at 77 K (the insets show pore size distribution profiles of **JNM-18** and **JNM-19** exhibiting a uniform pore size of 1.49 and 0.44 nm, respectively).

unit cell parameters of $a = b = 31.9432$ Å, and $c = 13.3836$ Å, and refinement parameters of $R_p = 3.40\%$ and $R_{wp} = 4.23\%$ (Fig. 2a). Similarly, structural simulation and PXRD experiment suggested that **JNM-19** employed AB staggered stacking mode of the 2D lamellar **kgd** layers, and Pawley refinement resulted in a hexagonal space group of $P6_3$ with unit cell parameters of $a = b = 31.6707$ Å, and $c = 12.5253$ Å, and refinement parameters of $R_p = 2.08\%$ and $R_{wp} = 2.62\%$ (Fig. 2d and e). Nitrogen adsorption measurements were performed at 77 K to study the porosities of **JNM-18** and **JNM-19**, where type I adsorption curves were found for both materials, indicating their microporous nature. Analyses of the Brunauer–Emmett–Teller (BET) surface areas afforded values of 761 and 596 m² g⁻¹ with total pore volumes of 0.4555 and 0.2836 ml g⁻¹ ($P/P_0 = 0.99$) for **JNM-18** and **JNM-19**, respectively. Moreover, narrow pore size distributions with peak values of 1.49 nm and 0.44 nm given by nonlocal density functional theory (NLDFT) for **JNM-18** and **JNM-19**, respectively, well agreed with the theoretical values of 1.47 and 0.42 nm found for the staggered AB stacking models of **JNM-18** and **JNM-19**, respectively (Fig. 2c and f).

The scanning electron microscopy (SEM) images of **JNM-18** showed ball-shape microcrystals with a nanometer size, while **JNM-19** exhibited flake-like morphologies in the micrometer range (Fig. 3a and d). High-resolution transmission electron microscopy (HR-TEM) images clearly exhibited highly crystalline nanolayers for the two materials (Fig. 3b and e), showing order lattice fringes with distances of 1.53 and 1.57 nm, respectively, associated with the (1$\bar{1}$0) and (110) planes for **JNM-18** and **JNM-19**, respectively (Fig. 3c and f).

**Optical and electrochemical properties**

The photocatalytic activities are significantly related to the relative energies of the band gap and their charge separation

efficiency. While **Cu₃L₃** showed light yellow color (Fig. S25†), **JNM-18** and **JNM-19** were obtained as yellow and green powder (Fig. S26 and S27†), respectively, suggesting stronger absorption of visible light for the D–A MOFs. The UV-Vis diffuse reflectance spectra of **JNM-18** and **JNM-19** exhibit more bathochromic absorption bands (Fig. 4a), resulting in reduced values of 2.61 and 2.84 eV, respectively, for the band gap energy, compared to that of **Cu₃L₃** (3.14 eV) based on the Kubelka–Munk equation (Fig. 4b). In addition, Mott–Schottky measurements showed positive slopes for **JNM-18** and **JNM-19**, indicative of typical n-type semiconductors, and the lowest unoccupied molecular orbital (LUMO) levels of **JNM-18** and **JNM-19** are estimated to be −1.04, and −1.14 eV *versus* Ag/AgCl, respectively (Fig. S28 and S29†). In consideration of the bandgaps obtained from the UV-vis spectra, the corresponding highest occupied molecular orbital (HOMO) levels of **JNM-18** and **JNM-19** are calculated to be +1.57, and +1.70 eV *versus* Ag/AgCl, respectively. The resulting band structures of **JNM-18** and **JNM-19** are therefore obtained, which clearly suggest they are capable of activating $O_2$ to superoxide anion radicals ($O_2^{\bullet-}$) which can be used in photocatalytic aerobic oxidation reactions (Fig. 4c).[25] Moreover, transient photocurrent responses were observed for **JNMs**, indicating the photo-induced charge separation (Fig. 4d). In contrast, **Cu₃L₃** showed negligible photocurrent response (Fig. S29†), suggesting that the construction of D–A networks with precise spatial distribution of donor and acceptor moieties could efficiently enhance the photo-induced charge separation.[15] Interestingly, the photocurrent intensity of **JNM-18** was higher than that of **JNM-19**, implying higher photo-induced charge separation efficiency of **JNM-18**. Furthermore, the electrochemical impedance spectroscopy (EIS) of **JNM-18** exhibited a smaller radius than that of **JNM-19**, suggesting a lower internal resistance for the

**Fig. 3** SEM images of **JNM-18** (a) and **JNM-19** (d). HR-TEM images of **JNM-18** (b) and **JNM-19** (e). Enlarged images of selected areas in part b (c) and e (f).



**Fig. 4** (a) UV-Vis diffuse reflectance spectra of **JNM-18**, **JNM-19** and **Cu₃L₃**. (b) Tauc plots of **JNM-18**, **JNM-19** and **Cu₃L₃** based on the UV-Vis diffuse reflectance spectra obtained from the Kubelka–Munk function. (c) Schematic depiction of pptical band gaps of **JNM-18** and **JNM-19**. (d) Photocurrent responses of **JNM-18** and **JNM-19**. (e) Electrochemical impedance spectra of **JNM-18** and **JNM-19**. (f) EPR spectra of **JNM-18** with DMPO in MeCN in the dark or under light irradiation.

charge transfer in **JNM-18** (Fig. 4e). Those optical and electrochemical experiments clearly reveal that the construction of D–A MOFs *via* direct imine linkage could reduce the band gap energy, resulting in the decrease of photocarrier transfer barrier and the increase of the charge separation efficiency.[39] Notably, **JNM-18** showed better photo-electrochemical properties than **JNM-19** that might be due to the stronger electron donating ability of the planar TPB units in the 2D networks, compared to the nonplanar HPB moieties with propeller

arrangement in **JNM-19**, which may enhance the photocatalytic activity of the materials.[37]

### Photocatalytic studies

With the remarkable photoelectronic properties of imine-linked D–A MOFs in hand, we elucidated their photocatalytic performance for the aerobic oxidation of amines to imines. Initially, the aerobic oxidation of benzylamine (**3a**) under light irradiation was chosen as a model reaction. As shown in

Table 1 (entry 1), when benzylamine (0.3 mmol) and 3 mol% (based on Cu) **JNM-18** were mixed in 2 mL CH$_3$CN and reacted at room temperature (rt) for 12 h under irradiation with a violet LED, compound **3a** underwent the oxidative coupling reaction to give the imine product (**4a**) with 94% yield confirmed by $^1$H NMR. To optimize the reaction conditions, several control experiments were conducted. In the absence of **JNM-18** or light irradiation, low conversion of **3a** was observed, suggesting the indispensability of catalysts and light in the aerobic oxidation reaction (Table 1, entries 2 and 3). Filled with Ar, the imine product **4a** was barely detected (Table 1, entry 4). With the use of O$_2$ instead of air, the conversion of **3a** could be increased to 99%, indicating the crucial role of O$_2$ as the terminal oxidant (Table 1, entry 5). Reaction solvents were found to strongly influence the photocatalytic efficiency, where the use of MeOH or EtOH instead of MeCN gave much lower yields (Table 1, entries 6 and 7). The use of a blue LED also resulted in much lower yield (Table 1, entry 8). The decrease of catalyst loading from 3 to 1.5 mol% reduced the coupling product yield to 61%, while the use of 6 mol% catalyst loading could not increase the yield (Table 1, entries 9 and 10). Reactions using **Cu$_3$L$_3$** afforded low yield, evidencing the significance of constructing D–A MOFs for improving the photocatalytic activity (Table 1, entry 11). Notably, when **JNM-19** was employed as a photocatalyst, **4a** with 75% or 92% yield can be obtained within 12 h or 24 h, respectively, suggesting a lower photocatalytic efficiency compared to **JNM-18** (Table 1, entries 12 and 13). This may due to the stronger electron donating ability arising from the planar TPB units in **JNM-18** frameworks than the nonplanar HPB moieties in **JNM-19**, which results in a larger photocarrier transfer barrier and lower

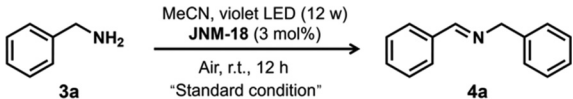charge separation efficiency, and thus enhanced photocatalytic performance.[40]

Superoxide anion radical (O$_2$$^{\bullet-}$) and singlet oxygen ($^1$O$_2$) are the ROS involved in the photocatalytic aerobic oxidation reaction.[25] Here, various control experiments were performed to study the generated ROS and the mechanism of the photocatalytic oxidation of **3a**. The addition of NaN$_3$ (5.0 equiv.) as the $^1$O$_2$ scavenger to the reaction solution did not change the conversion of **3a**, suggesting that $^1$O$_2$ was not involved in the reaction process (Table 1, entry 14). In contrast, the addition of benzoquinone (5.0 equiv.) as a O$_2$$^{\bullet-}$ scavenger remarkably lowered the yield to 5% (Table 1, entry 15). Besides, the use of AgNO$_3$ as an e$^-$ scavenger also impeded the oxidation of **3a** by disturbing the generation of O$_2$$^{\bullet-}$ from O$_2$ (Table 1, entry 16). Therefore, O$_2$$^{\bullet-}$ is the dominant ROS for **JNM-18** photocatalyzed aerobic oxidation reaction.

Moreover, we applied electron paramagnetic resonance (EPR) spectra to further investigate the ROS by spin trapping.[41] With the addition of 5,5-dimethyl-pyrroline-*N*-oxide (DMPO), the characteristic peaks of the DMPO–O$_2$$^{\bullet-}$ radical were found, of which the intensities were remarkably enhanced by prolonging the irradiation time, confirming the generation of O$_2$$^{\bullet-}$ active species by the **JNM-18** photocatalyst (Fig. 4f). Besides, the O$_2$$^{\bullet-}$ generation of **JNM-18** was further evaluated by the use of nitro blue tetrazolium (NBT), of which the absorption band at 259 nm was dramatically decreased upon the addition of **JNM-18** upon violet LED irradiation (Fig. S34†). The generation of O$_2$$^{\bullet-}$ ROS was also observed in **JNM-19** by EPR with DMPO and UV-vis spectroscopy with NBT (Fig. S31 and S34†), but with less efficiency than **JNM-18**. These results were consistent with the observation of lower conversion for the **JNM-19** photocatalyzed aerobic oxidation reaction.
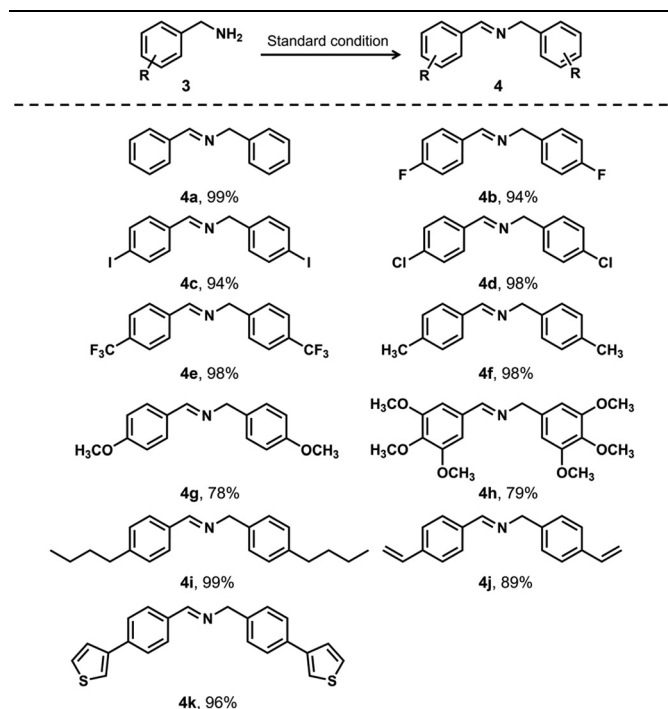
We also evaluate the reusability of **JNM-18** for heterogeneous photocatalyzed benzylamine oxidation reactions. Remarkably, the yields for the oxidative coupling products barely decreased (Fig. S35†). In addition, inductively coupled plasma mass spectrometry (ICP-MS) revealed that copper ions were not present in the reaction supernatant, suggesting that the photocatalyst **JNM-18** was not damaged after catalytic cycles (see the ESI† for details). Moreover, XPS analysis and PXRD measurement demonstrated the monovalent state of the Cu ions and high crystallinity of **JNM-18** remained during the recycle catalytic experiments (Fig. S36 and S37†). Furthermore, FT-IR spectra and SEM images of **JNM-18** before and after photocatalysis did not show obvious differences, implying the structural integrity (Fig. S38 and S39†).

Furthermore, we expanded the photocatalytic application using **JNM-18** by exploring various benzylamine derivatives with a broad range of substituents under the standard reaction conditions (Table 2). In general, the **JNM-18** photocatalyzed reaction was tolerant to different substituted primary amines, which were oxidized to the associated imines with excellent yields. Notably, the benzyl amines with electron-withdrawing groups exhibited higher yields (Table 2, entries 2–5), compared with those with electron-donating substituents (Table 2, entries 6–8), as a result of the enhanced electronegativity on

**Table 1** Control experiments for the photocatalytic oxidative coupling of benzylamine$^a$



| Entry | Change from the "standard conditions" | Yield (%) |
|---|---|---|
| 1 | None | 94 |
| 2 | No catalyst | 14 |
| 3 | No light | 4 |
| 4 | Under Ar, instead of air | Trace |
| 5 | Under O$_2$, instead of air | 99 |
| 6 | MeOH, instead of MeCN | 30 |
| 7 | EtOH, instead of MeCN | 34 |
| 8 | A blue LED, instead of a violet LED | 11 |
| 9 | 1.5 mol% **JNM-18** | 61 |
| 10 | 6 mol% **JNM-18** | 93 |
| 11 | **Cu$_3$L$_3$** instead of **JNM-18** | 10 |
| 12 | **JNM-19**, instead of **JNM-18** | 75 |
| 13 | **JNM-19**, instead of **JNM-18**, 24 h | 92 |
| 14 | NaN$_3$ as the $^1$O$_2$ scavenger | 92 |
| 15 | Benzoquinone as the O$_2$$^{\bullet-}$ scavenger | 5 |
| 16 | AgNO$_3$ as the e$^-$ scavenger | 5 |

$^a$ Reaction conditions: benzylamine (0.3 mmol), **JNM-18** (3 mol%), CH$_3$CN (2 mL), r.t., a violet LED (12 W), air. The reported yields presented are based on $^1$H NMR spectra.

This journal is © the Partner Organisations 2024

*Inorg. Chem. Front.*, 2024, **11**, 417–424 | **421**

**Table 2** Photocatalyzed aerobic oxidation of primary amines to imines by JNM-18 [a]



[a] Reaction conditions: amine (0.3 mmol), **JNM-18** (3 mol%), $CH_3CN$ (2 mL), rt, a violet LED (12 W), air. The reported yields presented are based on ^{1}H NMR spectra.

the benzyl moieties. Moreover, the steric effect using benzylamine substituted with a long alkyl chain was also tested, showing good yields for the corresponding imine product (Table 2, entry 9). Benzyl amines with reactive functional substituents, such as vinyl and thiophene, that may disturb the oxidation reactions were also applicable to the **JNM-18** photocatalyzed oxidation (Table 2, entries 10 and 11). We also investigated several secondary amines for the photocatalyzed oxidation to further explore the reaction scope (Table S5†). Though the yields were shown to be inferior to the reactions based on primary amines, the secondary amines could be oxidized to the corresponding imines, suggesting the good toleration in the aerobic oxidation of amines using the **JNM-18** photocatalyst.

Gradually, a plausible mechanism for the photocatalyzed aerobic oxidation of benzylamine by the CTU-based D–A MOFs is proposed on the basis of the above experimental data and reported results in the literature (Fig. S40†).[14,15,38,41–45] Taking **JNM-18** as an example, the D–A MOF plays a role as a transfer channel that accelerates the separation of electron–hole systems ($e^-$–$h^+$) upon irradiation with violet light, following the singlet electron transfer (SET) which migrated $e^-$ from the HOMO to the LUMO in **JNM-18** and generated $O_2^{\bullet-}$ by reduction of $O_2$. Secondly, benzylamine was rapidly transformed to the amine radical cation by $h^+$ drifted on the **JNM-18** surface, which subsequently reacted with $O_2^{\bullet-}$ to form

the benzaldimine intermediate that further condenses with benzylamine to generate the target product.

## Conclusions

In summary, two imine-linked D–A MOFs, **JNM-18** and **JNM-19**, were reticularly synthesized by covalent networking of Cu(I) CTUs and an organic linker functionalized with TPB and HPB electron-donating moieties, respectively. The obtained D–A MOFs show high crystallinity and uniform porosity. In addition, due to the precise spatial distribution of donor and acceptor units within the extended networks, the D–A MOFs exhibited excellent photocatalytic performance for the aerobic oxidation reaction of benzylamines upon photo-irradiation. Moreover, **JNM-18** exhibited stronger visible-light absorption, higher charge separation efficiency, and higher ROS generation efficiency compared to **JNM-19**, thus resulting in higher photocatalytic activity. This work demonstrates a facile approach to synthesize D–A MOFs by reticular chemistry of dynamic covalent bonds, which is helpful for developing and designing efficient MOF photocatalysts.

## Author contributions

R.-J. W., G.-H. N. and D. L. designed the research; R.-Q. X., T.-E. Z. and Z.-N. L. conducted the experiments and data analysis; R.-Q. X., R.-J. W., G.-H. N. and D. L. co-wrote the manuscript. All authors read and commented on the manuscript.

## Conflicts of interest

There are no conflicts to declare.

## Acknowledgements

## References

1 O. M. Yaghi, M. O'Keeffe, N. W. Ockwig, H. K. Chae, M. Eddaoudi and J. Kim, Reticular Synthesis and the Design of New Materials, *Nature*, 2003, **423**, 705–714.

2 M. Li, D. Li, M. O'Keeffe and O. M. Yaghi, Topological Analysis of Metal–Organic Frameworks with Polytopic

**422** | *Inorg. Chem. Front.*, 2024, **11**, 417–424

This journal is © the Partner Organisations 2024

Linkers and/or Multiple Building Units and the Minimal Transitivity Principle, *Chem. Rev.*, 2014, **114**, 1343–1370.

3  A. Schoedel, M. Li, D. Li, M. O'Keeffe and O. M. Yaghi, Structures of Metal–Organic Frameworks with Rod Secondary Building Units, *Chem. Rev.*, 2016, **116**, 12466–12535.

4  H. Zeng, M. Xie, T. Wang, R.-J. Wei, X.-J. Xie, Y. Zhao, W. Lu and D. Li, Orthogonal-Array Dynamic Molecular Sieving of Propylene/Propane Mixtures, *Nature*, 2021, **595**, 542–548.

5  R.-B. Lin, S. Xiang, W. Zhou and B. Chen, Microporous Metal–Organic Framework Materials for Gas Separation, *Chem*, 2020, **6**, 337–363.

6  A. J. Rieth, A. M. Wright and M. Dincă, Kinetic Stability of Metal–Organic Frameworks for Corrosive and Coordinating Gas Capture, *Nat. Rev. Mater.*, 2019, **4**, 708–725.

7  Z. Han, Z. Yan, K. Wang, X. Kang, K. Lv, X. Zhang, Z. Zhou, S. Yang, W. Shi and P. Cheng, Observation of Oxygen Evolution over a {Ni$_{12}$}-Cluster Based Metal-Organic Framework, *Sci. China: Chem.*, 2022, **65**, 1088–1093.

8  C. Fiankor, J. Nyakuchena, R. S. H. Khoo, X. Zhang, Y. Hu, S. Yang, J. Huang and J. Zhang, Symmetry-Guided Synthesis of N, N′-Bicarbazole and Porphyrin-Based Mixed-Ligand Metal–Organic Frameworks: Light Harvesting and Energy Transfer, *J. Am. Chem. Soc.*, 2021, **143**, 20411–20418.

9  H. Miyasaka, Control of Charge Transfer in Donor/Acceptor Metal–Organic Frameworks, *Acc. Chem. Res.*, 2013, **46**, 248–257.

10 B. Zhang, J. Xu, C. T. Li, H. L. Huang, M. X. Chen, M. H. Yu, Z. Chang and X. H. Bu, Facile Tuned TSCT-TADF in Donor-Acceptor MOF for Highly Adjustable Photonic Modules Based on Heterostructures Crystals, *Angew. Chem., Int. Ed.*, 2023, **62**, e202303262.

11 D. S. Zhang, Q. Gao, Z. Chang, X. T. Liu, B. Zhao, Z. H. Xuan, T. L. Hu, Y. H. Zhang, J. Zhu and X. H. Bu, Rational Construction of Highly Tunable Donor-Acceptor Materials Based on a Crystalline Host-Guest Platform, *Adv. Mater.*, 2018, **30**, 1804715.

12 E. Romero, J. R. Gómez Castellanos, G. Gadda, M. W. Fraaije and A. Mattevi, Same Substrate, Many Reactions: Oxygen Activation in Flavoenzymes, *Chem. Rev.*, 2018, **118**, 1742–1769.

13 F. Zhang, J. Ma, Y. Tan, G. Yu, H. Qin, L. Zheng, H. Liu and R. Li, Construction of Porphyrin Porous Organic Cage as a Support for Single Cobalt Atoms for Photocatalytic Oxidation in Visible Light, *ACS Catal.*, 2022, **12**, 5827–5833.

14 K. Wu, X.-Y. Liu, P.-W. Cheng, M. Xie, W. Lu and D. Li, Metal-Organic Frameworks as Photocatalysts for Aerobic Oxidation Reactions, *Sci. China: Chem.*, 2023, **66**, 1634–1653.

15 K. Wu, X.-Y. Liu, P.-W. Cheng, Y.-L. Huang, J. Zheng, M. Xie, W. Lu and D. Li, Linker Engineering for Reactive Oxygen Species Generation Efficiency in Ultra-Stable Nickel-Based Metal–Organic Frameworks, *J. Am. Chem. Soc.*, 2023, **145**, 18931–18938.

16 Z. W. Jiang, Y. C. Zou, T. T. Zhao, S. J. Zhen, Y. F. Li and C. Z. Huang, Controllable Synthesis of Porphyrin-Based 2D Lanthanide Metal–Organic Frameworks with Thickness– and Metal–Node–Dependent Photocatalytic Performance, *Angew. Chem., Int. Ed.*, 2020, **59**, 3300–3306.

17 J.-K. Jin, K. Wu, X.-Y. Liu, G.-Q. Huang, Y.-L. Huang, D. Luo, M. Xie, Y. Zhao, W. Lu and X.-P. Zhou, Building a Pyrazole–Benzothiadiazole–Pyrazole Photosensitizer into Metal–Organic Frameworks for Photocatalytic Aerobic Oxidation, *J. Am. Chem. Soc.*, 2021, **143**, 21340–21349.

18 J. Zheng, Z. Lu, K. Wu, G. H. Ning and D. Li, Coinage-Metal-Based Cyclic Trinuclear Complexes with Metal-Metal Interactions: Theories to Experiments and Structures to Functions, *Chem. Rev.*, 2020, **120**, 9675–9742.

19 Y.-M. Wang, K.-M. Mo, X. Luo, R.-Q. Xia, J.-Y. Song, G.-H. Ning and D. Li, An Anthraquinone-Based Cu(ı) Cyclic Trinuclear Complex for Photo-Catalyzing C-C Coupling Reactions, *Sci. China: Chem.*, 2023, **66**, DOI: 10.1007/s11426-023-1777-y.

20 A. P. Côté, A. I. Benin, N. W. Ockwig, M. O'Keeffe, A. J. Matzger and O. M. Yaghi, Porous, Crystalline, Covalent Organic Frameworks, *Science*, 2005, **310**, 1166–1170.

21 R.-J. Wei, H.-G. Zhou, Z.-Y. Zhang, G.-H. Ning and D. Li, Copper(ı)–Organic Frameworks for Catalysis: Networking Metal Clusters with Dynamic Covalent Chemistry, *CCS Chem.*, 2020, **2**, 2045–2053.

22 H.-G. Zhou, R.-Q. Xia, J. Zheng, D. Yuan, G.-H. Ning and D. Li, Acid-Triggered Interlayer Sliding of Two-Dimensional Copper(ı)–Organic Frameworks: More Metal Sites for Catalysis, *Chem. Sci.*, 2021, **12**, 6280–6286.

23 X.-C. Lin, Y.-M. Wang, X. Chen, P.-Y. You, K.-M. Mo, G.-H. Ning and D. Li, A Photosensitizing Metal-Organic Framework as a Tandem Reaction Catalyst for Primary Alcohols from Terminal Alkenes and Alkynes, *Angew. Chem., Int. Ed.*, 2023, **62**, e202306497.

24 H. L. Nguyen, F. Gándara, H. Furukawa, T. L. Doan, K. E. Cordova and O. M. Yaghi, A Titanium–Organic Framework as an Exemplar of Combining the Chemistry of Metal– and Covalent–Organic Frameworks, *J. Am. Chem. Soc.*, 2016, **138**, 4330–4333.

25 J. Luo, X. Luo, M. Xie, H.-Z. Li, H. Duan, H.-G. Zhou, R.-J. Wei, G.-H. Ning and D. Li, Selective and Rapid Extraction of Trace Amount of Gold from Complex Liquids with Silver(ı)-Organic Frameworks, *Nat. Commun.*, 2022, **13**, 7771.

26 J. Zhou, J. Li, L. Kan, L. Zhang, Q. Huang, Y. Yan, Y. Chen, J. Liu, S.-L. Li and Y.-Q. Lan, Linking Oxidative and Reductive Clusters to Prepare Crystalline Porous Catalysts for Photocatalytic CO$_2$ Reduction with H$_2$O, *Nat. Commun.*, 2022, **13**, 4681.

27 J.-N. Lu, J.-J. Liu, L.-Z. Dong, J.-M. Lin, F. Yu, J. Liu and Y.-Q. Lan, Synergistic Metal–Nonmetal Active Sites in a Metal–Organic Cage for Efficient Photocatalytic Synthesis of Hydrogen Peroxide in Pure Water, *Angew. Chem.*, 2023, **63**, e202308505.

28 X. Wang, X. Ding, Y. Jin, D. Qi, H. Wang, Y. Han, T. Wang and J. Jiang, Post-Nickelation of a Crystalline Trinuclear Copper Organic Framework for Synergistic Photocatalytic Carbon Dioxide Conversion, *Angew. Chem., Int. Ed.*, 2023, **62**, e202302808.

29 R.-J. Wei, M. Xie, R.-Q. Xia, J. Chen, H.-J. Hu, G.-H. Ning and D. Li, Gold(I)-Organic Frameworks as Catalysts for Carboxylation of Alkynes with $CO_2$, *J. Am. Chem. Soc.*, 2023, **145**, 22720–22727.

30 J. Zheng, H. Yang, M. Xie and D. Li, The π-Acidity/Basicity of Cyclic Trinuclear Units (CTUs): From a Theoretical Perspective to Potential Applications, *Chem. Commun.*, 2019, **55**, 7134–7146.

31 R.-Q. Xia, J. Zheng, R.-J. Wei, J. He, D.-Q. Ye, M.-D. Li, G.-H. Ning and D. Li, Strong Visible Light-Absorbing Bodipy-Based Cu(I) Cyclic Trinuclear Sensitizer for Photocatalysis, *Inorg. Chem. Front.*, 2022, **9**, 2928–2937.

32 C. Mejuto, G. Guisado-Barrios, D. Gusev and E. Peris, First Homoleptic MIC and Heteroleptic NHC–MIC Coordination Cages from 1,3,5-Triphenylbenzene-Bridged Tris-MIC and Tris-NHC Ligands, *Chem. Commun.*, 2015, **51**, 13914–13917.

33 Y. Zhang, G. Wu, H. Liu, R. Tian, Y. Li, D. Wang, R. Chen, J. Zhao, S. Liu and Z. Li, Donor–Acceptor Based Two-Dimensional Covalent Organic Frameworks for near-Infrared Photothermal Conversion, *Mater. Chem. Front.*, 2021, **5**, 6575–6581.

34 S. Pramanik, H. Deol, V. Bhalla and M. Kumar, Aiee Active Donor–Acceptor–Donor-Based Hexaphenylbenzene Probe for Recognition of Aliphatic and Aromatic Amines, *ACS Appl. Mater. Interfaces*, 2017, **10**, 12112–12123.

35 H. Liu, Z. Zhang, C. Mu, L. Ma, H. Yuan, S. Ling, H. Wang, X. Li and M. Zhang, Hexaphenylbenzene-Based Deep Blue-Emissive Metallacages as Donors for Light-Harvesting Systems, *Angew. Chem., Int. Ed.*, 2022, **61**, e202207289.

36 R. Rathore, C. L. Burns and S. A. Abdelwahed, Hopping of a Single Hole in Hexakis [4-(1, 1, 2-Triphenyl-Ethenyl) Phenyl] Benzene Cation Radical through the Hexaphenylbenzene Propeller, *Org. Lett.*, 2004, **6**, 1689–1692.

37 K. Xiong, Y. Wang, F. Zhang, X. Li and X. Lang, Linker Length-Dependent Photocatalytic Activity of β-Ketoenamine Covalent Organic Frameworks, *Appl. Catal., B*, 2023, **322**, 122135.

38 H. Duan, X. Chen, Y.-N. Yang, J. Zhao, X.-C. Lin, W.-J. Tang, Q. Gao, G.-H. Ning and D. Li, Tailoring Stability, Catalytic Activity and Selectivity of Covalent Metal–Organic Frameworks Via Steric Modification of Metal Nodes, *J. Mater. Chem. A*, 2023, **11**, 12777–12783.

39 P. You, R. Wei, G. Ning and D. Li, An Eosin Y Encapsulated Cu(I) Covalent Metal Organic Framework for Efficient Photocatalytic Sonogashira Cross-Coupling Reaction, *Chem. Res. Chin. Univ.*, 2022, **38**, 415–420.

40 J.-D. Yi, R. Xu, Q. Wu, T. Zhang, K.-T. Zang, J. Luo, Y.-L. Liang, Y.-B. Huang and R. Cao, Atomically Dispersed Iron–Nitrogen Active Sites within Porphyrinic Triazine-Based Frameworks for Oxygen Reduction Reaction in Both Alkaline and Acidic Media, *ACS Energy Lett.*, 2018, **3**, 883–889.

41 K. Wu, X.-Y. Liu, M. Xie, P.-W. Cheng, J. Zheng, W. Lu and D. Li, Rational Design of D-π-A-π-D Porous Organic Polymer with Polarized π for Photocatalytic Aerobic Oxidation, *Appl. Catal., B*, 2023, **334**, 122847.

42 H. Wei, Z. Guo, X. Liang, P. Chen, H. Liu and H. Xing, Selective Photooxidation of Amines and Sulfides Triggered by a Superoxide Radical Using a Novel Visible-Light-Responsive Metal–Organic Framework, *ACS Appl. Mater. Interfaces*, 2019, **11**, 3016–3023.

43 H. Liu, Z. Guo, H. Lv, X. Liu, Y. Che, Y. Mei, R. Bai, Y. Chi and H. Xing, Visible-Light-Driven Self-Coupling and Oxidative Dehydrogenation of Amines to Imines via a Mn (II)-Based Coordination Polymer, *Inorg. Chem. Front.*, 2020, **7**, 1016–1025.

44 K. Gao, H. Li, Q. Meng, J. Wu and H. Hou, Efficient and Selective Visible-Light-Driven Oxidative Coupling of Amines to Imines in Air over CdS@ Zr-MOFs, *ACS Appl. Mater. Interfaces*, 2021, **13**, 2779–2787.

45 W.-J. Xu, B.-X. Huang, G. Li, F. Yang, W. Lin, J.-X. Gu, H.-G. Deng, Z.-G. Gu and H.-G. Jin, Donor–Acceptor Mixed-Naphthalene Diimide-Porphyrin MOF for Boosting Photocatalytic Oxidative Coupling of Amines, *ACS Catal.*, 2023, **13**, 5723–5732.

**424** | *Inorg. Chem. Front.*, 2024, **11**, 417–424

This journal is © the Partner Organisations 2024